Structure-dynamics relationship in Al-Mg-Si liquid alloys

Alaa Fahs [1,2] Philippe Jarry,[1,2] and Noël Jakse [1]

[1]*Univ. Grenoble Alpes, CNRS, Grenoble INP, SIMaP, F-38000 Grenoble, France*
[2]*C-TEC, Parc Economique Centr'alp, 725 rue Aristide Bergès, CS10027, Voreppe 38341 Cedex, France*

Enhancing properties and performances of aluminium alloys by control of their solidification is pivotal in the automotive and aerospace industries. The fundamental role of the structure-diffusion relationship is investigated for Al-Mg-Si liquid alloys taken as a prototype of Al-6xxx. For this purpose, first principles based molecular dynamics simulations were performed for various Si and Mg content for Al-rich compositions, including the binary alloy counterparts. Results indicate that Mg and/or Si in alloys create a more compact ordering around Al in the alloy than the one existing in pure Al, thus lowering diffusion. Mg promotes icosahedral short-range order, while Si displays a preference towards cubic local ordering, impacting diffusion based on their respective content. It suggests a mechanism whereby an increase in Mg content generally lowers the diffusion of each species, whereas an increase in Si content enhances their diffusion, providing insights for future alloy design.

I. INTRODUCTION

Aluminium alloys represent one of the main categories of structural metallic materials widely utilized in automotive construction and the aerospace industries [1–5]. They are attractive due to their high strength-to-density ratio, functional extrudability, age hardening characteristics, excellent corrosion resistance, as well as surface and welding properties. Moreover, the possibility of an almost complete recycling is a strong argument from an environmental point of view. Controlling properties and improving quality and performance of Al-based alloys represent timely and major industrial challenges [6,7].

Improvements can be possible through controlled modification of the targeted microstructure. This requires a good understanding of solidification, a nonequilibrium process governed by the trade-off between solute diffusion in the liquid phase, crystal-liquid interfacial energy and anisotropy [8]. Unfortunately, experimental data for self-diffusion in liquid metals are scarce and most of them related to monatomic liquid metal, mainly due to a lack of specific radioisotopes [9]. Alternatively, inserting the experimental viscosity data, widely available in the literature, into phenomenological laws such as the Stokes-Einstein (SE) equation [10,11], could indirectly give a rough estimation of solute diffusivity. However, this approximated method happens to fail in most of the cases for multi-component liquid alloys. It might be due to a possible different local ordering around each species [12,13], which falls out of the assumption of the SE relation, and does not extend to undercooling conditions where solidification occurs.

Similarities in densities and coordination numbers between the liquid and crystal, for instance, led to the recognition that the local atomic ordering, known as the short-range order (SRO), might be different from the one leading to the long-range crystalline structure [14]. Frank [15] was the first to show that the icosahedral ordering is locally more stable. This might engender complex situations in the undercooled melt in terms of the variety of polymorphs [16], competing short range orders [17–19], or an interplay between chemical and fivefold symmetry (FFS) orderings in liquid alloys [20–22] prior to nucleation. More precisely, the proportion of atom pairs belonging to icosahedral short-range order (ISRO) strongly depends upon the nature of the solutes. In particular, in the $Al_{93}Cr_7$ liquid alloy, *ab initio* molecular dynamics (AIMD) calculations showed the existence of an onset of icosahedral medium-range order (IMRO), induced by the interplay between chemical short-range order (CSRO) and ISRO. This leads to dynamical heterogeneities (DHs) characterized by a strong heterogeneity in the propension to diffuse [21,23]. Another AIMD study of the liquid $Al_{1-x}Ni_x$ alloy pointed out the existence of a nonlinear evolution with composition x of dynamic properties due to nonlinear composition dependence of CSRO [24]. More generally, a deeper understanding of the structure-dynamic relationship in liquid metals and alloys is needed for designing alloys with desired properties.

In this context, the possibility of calculating dynamic properties together with the underlying structure in the liquid and undercooled states on the same footing can be provided by *ab initio* molecular dynamics [12,13,20,21,23–33]. For most metallic systems, AIMD is able to accurately account for interatomic interactions on the basis of the density functional theory (DFT) [34]. Despite the heaviness of the underlying quantum computation to get the electronic structure, AIMD simulations currently allow us to build phase space trajectories of system sizes of the order of 10^2 atoms over several hundreds of picoseconds [21], relevant for the determination of diffusion coefficients for all species. Another strategy consists in developing Machine learning (ML) interatomic potentials trained on an appropriate set of AIMD configurations, allowing to perform up to million-atom molecular dynamics (MD) simulations with an accuracy close to *ab initio* [35]. It should be noted that ML potentials for aluminium and its alloys in the liquid and solid states were proposed recently [36–38] and used to study early stage of solidification [37].

The present work aims at investigating the structure-dynamic relationships in liquid and undercooled Al-Mg-Si ternary alloys, which are prototypical to the Al-based 6xxx used in the automobile industry. For this purpose, *ab initio* molecular dynamics are performed for various Al-rich compositions, namely, $Al_{80}Mg_{10}Si_{10}$, $Al_{70}Mg_{20}Si_{10}$, and $Al_{70}Mg_{10}Si_{20}$. In particular, the addition of Mg and Si in liquid aluminium is further quantified by performing also AIMD simulations for $Al_{90}Mg_{10}$ and the $Al_{90}Si_{10}$ binary counterparts to disentangle effects of Mg and Si in the ternary liquid alloys. It should be mentioned that these compositions have a higher Si and Mg content than the 6xxx Alloys. This choice was made given the small size of the simulation boxes, and intends to highlight the generic relationship between local atomic ordering and the dynamics. Besides, due to eutectic solute partitioning upon crystallization, the local liquid composition is significantly higher at the solid-liquid interface than in the liquid bulk, typically by a factor 3 for Mg and 10 for Si, which makes the compositions studied here relevant. Our results show significant structural heterogeneities with Mg or Si addition in aluminium either in binary or ternary alloys. In all cases, an enhancement of the FFS around Mg atoms is observed, while a decrease is seen around Si, leading to a decoupling of diffusion. Impact of these findings on the early stages of solidification in the alloys is further discussed.

The layout of the paper is the following. Section II is devoted to the computational aspects of the work, Sec. III shows results of structural and dynamic properties along with a discussion of the interplay between the local structural properties and the dynamics, and finally, Sec. IV draws the conclusions.

II. COMPUTATIONAL BACKGROUND

A. *Ab initio* molecular dynamics

The structure and dynamic properties of binary $Al_{90}Mg_{10}$ and $Al_{90}Si_{10}$, as well as ternary $Al_{80}Mg_{10}Si_{10}$, $Al_{70}Mg_{20}Si_{10}$, and $Al_{70}Mg_{10}Si_{20}$ liquid alloys, were determined by means of *ab initio* molecular dynamics simulations within the density functional theory, using the Vienna *ab initio* simulation package (VASP) [39]. Projected augmented-wave method was used to describe the electron-ion interaction [40], with a plane wave cutoff of 250 eV and only the Γ point to sample the Brillouin zone. Exchange and correlation effects were taken into account through the Local density approximation (LDA) [41]. As a matter of fact, it was shown in preceding works that the LDA, among other functionals, gives the best representation of the structure and diffusion coefficients with respect to experiments in pure Al and Al-rich alloys in the liquid and undercooled states [23,33,42,43].

The phase space trajectories were constructed through dynamical simulations by numerical integration of Newton's equation of motion using the standard Verlet algorithm [44] in the velocity form with a time step of 1.5 fs. All simulations were done in a cubic box of $N = 256$ atoms with periodic boundary conditions in the three directions of space. The number of each species in all the simulations can be found in Table I in Ref. [45] (see also Refs. [33,37,43,46–48] therein). For each simulation, the volume V was adjusted to reach pressure with an uncertainty less than 0.5 GPa, which is of the order of pressure fluctuations (see Fig. S1 in Ref. [45]). In order to

control the temperature T, the simulations were performed in the canonical ensemble (constant N, V, and T) with a Nosé thermostat [49]. Thermalization was carried out for at least 20 ps, according to the relaxation time evaluated from the self-intermediate scattering function $F_S(q, t)$ [50], that are given in Table 4 in Ref. [45]. Simulations were continued during 60 to 160 ps with decreasing temperature, in order to extract the structural and dynamic properties with a sufficient statistics. The temperature evolution in the undercooled states was obtained by quenching the system step-wise down to 600 K with a temperature step of 100 K from an equilibrated state at the previous temperature, resulting in an average quenching rate of 10^{13} K/s.

From equilibrated trajectories at each temperature, a regular sampling of 10 configurations was performed to obtain the inherent structure (IS) configuration [51], from which a structural analysis is extracted by means of the Common-neighbor analysis (CNA) [52] using PYTHON modules of the Open VIsualization TOol (OVITO) [53]. To this end, static relaxation simulations were performed for each of these configurations, performing an energy minimization procedure with the conjugate gradient method. This procedure is important to uncouple the vibrational motion from the underlying structural properties by bringing atoms to a local minimum in the potential-energy surface and reduce the noise in the CNA index calculations.

B. Structural and dynamic properties

Structural properties were first investigated through the calculation of the total structure factor using the Debye equation for the purpose of comparing the simulation results to existing experimental measurements:

$$S(q) = \frac{1}{N} \sum_{j,k} b_j b_k \langle e^{i\mathbf{q}[\mathbf{r}_j - \mathbf{r}_k]} \rangle, \qquad (1)$$

where $\mathbf{q}$ is the wave vector, b_j and $\mathbf{r_j}$ represent respectively the neutron or x-ray scattering length, and the position of the atom j, and the angle brackets denote averaging over configurations sampled along the phase-space trajectory. The partial structural factors were calculated in the same manner within the Faber-Ziman formalism [46].

The partial pair-correlation functions $g_{ij}(r)$ were also considered to give a view of the local structural properties in the real space. These functions are written as

$$g_{ij}(r) = \frac{V}{N_i 4\pi r^2} \lim_{\Delta r \to 0} \frac{n_{ij}(r + \Delta r)}{\Delta r}, \qquad (2)$$

where i and j refer to two different types of atoms, N_i is the number of atoms of type i, $n_{ij}(r)$ is the mean number of atoms of type j around an atom of type i in a spherical shell of radius r and thickness Δr centered on an atom i taken as the origin. The corresponding partial coordination numbers or the number of first nearest neighbors of a reference atom was calculated using the following equation:

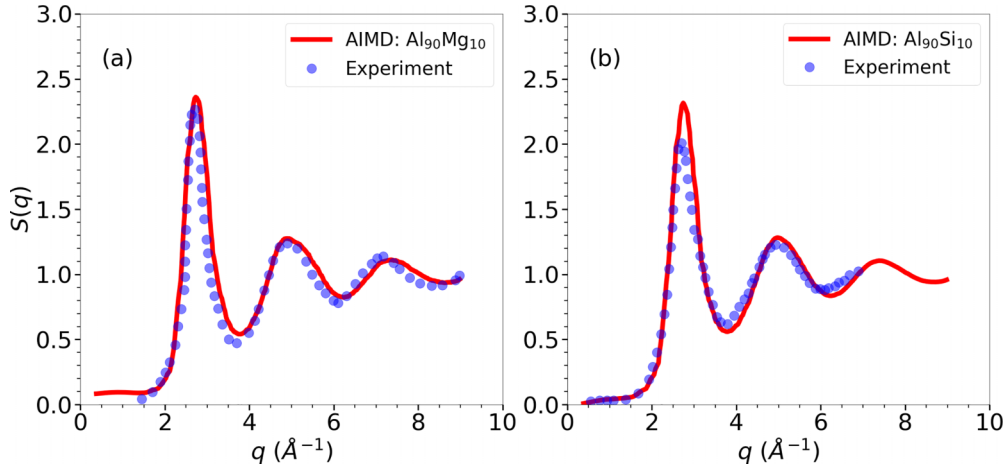$$N_{ij} = \rho_j \int_0^{r_{min}} 4\pi r^2 g_{ij}(r) dr, \qquad (3)$$

FIG. 1. AIMD calculations of the total x-ray structure factors in liquid $Al_{90}Mg_{10}$ (a) and $Al_{90}Si_{10}$ (b) (solid lines), at temperature $T = 1000$ and 900 K, respectively. Experimental data are shown with the symbols [47,55] for comparison.

where $\rho_j = N_j/V$ is the partial number density, and r_{min} corresponds to the distance at the first minimum of the corresponding partial pair-correlation function $g_{ij}(r)$.

The local ordering surrounding each pair of atoms is further investigated through common-neighbor analysis (CNA), which is able to discriminate between various local topologies like cubic, namely fcc and bcc, hexagonal such as hcp, icosahedral ordering referred hereafter as FFS, or ISRO, as well as more complex environments like the Frank-Kasper polytetrahedral arrangements. The classification of each pair of atoms according to the number and topology of their common neighbors is done by means of a set of three indices in the Faken and Jonsson [52] nomenclature. For example, a bulk fcc crystal signature is 421, the hcp one contains the same pair as well as an additional 422 pair in equal proportion. The 444 pair together with the 666 one is a signature typical of the bulk bcc crystals with proportion 6/14 and 8/14, respectively. On the other hand, the 555 pair, corresponding to a pentagonal bipyramid, is characteristic of icosahedral order, with distortion thereof signaled by the presence of 544 and 433 pairs.

The diffusion of an atom of type i can be tracked by means of the mean-square-displacement as function of time t, which is written as follows:

$$R_i^2(t) = \frac{1}{N_i} \sum_{k=1}^{N_i} \langle [\mathbf{r}_k(t+t_0) - \mathbf{r}_k(t_0)]^2 \rangle_{t_0}, \tag{4}$$

where the angular brackets represent an averaging over time origins t_0. Then, partial diffusion coefficients D_i could be deduced from $R_i^2(t)$ as follows:

$$D_i = \lim_{t \to +\infty} \frac{R_i^2(t)}{6t}. \tag{5}$$

The diffusion coefficient were systematically corrected using the scheme of Yeh and Hummer [54] to take finite size effects into account, with an estimation of the viscosity of pure Al [33].

The individual atomic dynamics in liquids is also inspected through the self-intermediate scattering function (SISF) and the non-Gaussian parameter (NGP). The former, which reads

$$F_S(\mathbf{q}, t) = \frac{1}{N} \left\langle \sum_{i=1}^N e^{-i\mathbf{q}\cdot[\mathbf{r}_i(t_0+t)-\mathbf{r}_i(t_0)]} \right\rangle, \tag{6}$$

provides insights into the temporal evolution of the spatial correlations of individual atoms and describes how the position of a particle correlates in time. $F_S(\mathbf{q}, t)$ starts at 1 when $t = 0$ and decays to 0 at long time, atoms being totally uncorrelated with their initial positions. The value at $1/e$ is taken as a definition of structural relaxation time τ_s. The non-Gaussian parameter is defined as

$$\alpha_2(t) = \frac{3\langle R^4(t) \rangle}{5\langle R^2(t) \rangle^2} - 1, \tag{7}$$

where the angular brackets stand for the average over time origins of the total mean-square displacement $R^2(t)$ and total mean-quartic displacement

$$R^4(t) = \frac{1}{N} \sum_{k=1}^N \langle [\mathbf{r}_k(t+t_0) - \mathbf{r}_k(t_0)]^4 \rangle_{t_0}. \tag{8}$$

For a Gaussian diffusion process, i.e., homogeneous, this parameter is zero. Positive values indicate a deviation from Gaussian diffusive behavior and thus are interpreted as the presence of dynamic heterogeneities within the system.

C. Comparison with experiments

First of all, the reliability of our *ab initio* calculations is assessed by comparing calculated total structure factors $S(q)$ with existing experimental data [47,55]. Figures 1(a) and 1(b) show AIMD results for $Al_{90}Mg_{10}$ and $Al_{90}Si_{10}$ liquid alloys at temperatures $T = 1000$ and 900 K, respectively. A good agreement is obtained with x-ray diffraction data [47,55] regarding the position and amplitude of the first peak and subsequent oscillations. Moreover, Al-Mg and Mg-Mg partial structure factors in liquid $Al_{90}Mg_{10}$ are compared to experimental data of Waseda [47] in Fig. S2 in Ref. [45] within the Faber-Ziman formalism [46]. The Mg-Mg partial structure factor is well reproduced. This is all the more true for Al-Mg partial, especially regarding the peak positions, even if their amplitude
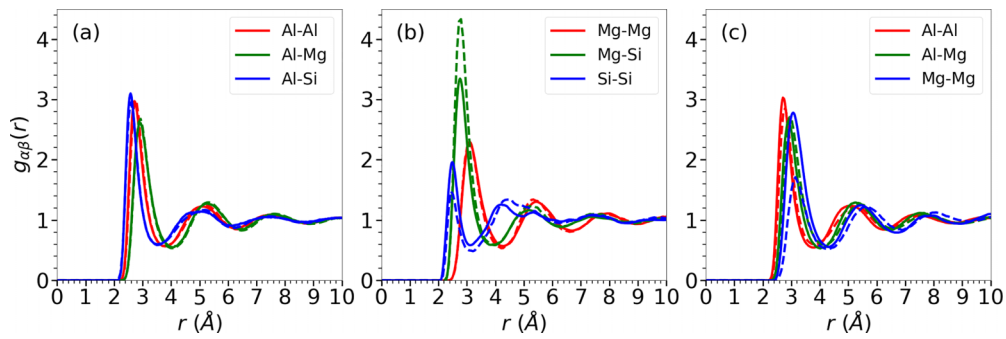
FIG. 2. Partial pair-correlation functions of $Al_{80}Mg_{10}Si_{10}$ (a) and (b) as well as $Al_{90}Mg_{10}$ (c) at $T = 1000$ K. HDNNP results (dashed lines) are compared to AIMD data (solid lines).

is a bit underestimated. Such a result is particularly remarkable given the experimental difficulties to extract partials. To the best of our knowledge, no experimental data were reported ti date in the literature for the ternary Al-Mg-Si liquid alloys.

D. Comparison with machine learning potentials

Machine learning interatomic potentials were developed recently for the Al-Mg-Si ternary system [38] using a High Dimensional Neural Network Potential (HDNNP) [56]. Using the version named NN-19, extracted from the Materials Cloud [38], local structural and diffusion properties were carried out by molecular dynamics (MD) using LAMMPS in the same conditions as our AIMD calculations. The use of HDNNP was possible by means of the library-based implementation n2p2 by Singraber *et al.* [57].

Partial pair-correlation functions of $Al_{80}Mg_{10}Si_{10}$ liquid alloy from HDNNP at $T = 1000$ K are plotted in Figs. 2(a) and 2(b). As a general trends, AIMD curves are well reproduced by the HDNNP, especially for Al-Al, Al-Mg and Al-Si pairs. Only the first peak of the Mg-Si partial shows an overestimated amplitude, and thus a higher Mg-Si affinity. More importantly, diffusion coefficients shown in Fig. S3 in Ref. [45], are in good agreement with AIMD in the liquid and undercooled states. This demonstrates the reliability of this potential and opens the way to larger scale simulations for early stage of solidification, with close to *ab initio* accuracy in the range of compositions studied here. The $Al_{90}Mg_{10}$ and $Al_{90}Si_{10}$ binary counterparts of the Al-Mg-Si ternary system were also investigated with the HDNNP. Figure 2(c) comparison with AIMD for $Al_{90}Mg_{10}$, where a good agreement is seen. However, the self-diffusion coefficients reported in Fig. S4 [45] show increasing departure with temperature, yet keeping the correct hierarchy $D_{Mg} < D_{Al}$. For $Al_{90}Si_{10}$ it was not possible to run stable MD simulations in the liquid state. The HDNNP for the ternary Al-Mg-Si ternary system is seemingly not completely transferable to binary counterparts. Training set should include the corresponding binary alloys, and the monoatomic metals if it were to be used for studying solidification phenomena.

III. RESULTS

A. Structural properties

The local structural properties are first considered through the partial pair correlation functions calculated from the AIMD simulations using Eq. (2). They are shown in

Figs. 3(a)–3(f) for the $Al_{80}Mg_{10}Si_{10}$ ternary liquid alloy. The first peak position of each partial reflects the first neighbor average distances, and thus the bonding length between the corresponding type of pairs. Going from the liquid state close to the liquidus at $T = 1000$ K to the undercooled states at $T = 600$ K, the first peak does not change significantly in its position whatever the partial. Nevertheless, its height increases visibly, showing that the short-range order becomes more and more pronounced and well defined. This is all the more true for the second oscillation whose amplitude increases. Moreover, for Al-Al, Al-Si and Al-Mg partials it splits in two sub-peaks or displays a shoulder, a feature that is often attributed to the reinforcement of the FFS [21,24,32,33,58,59]. Figure 3(f) shows that the amplitude of the $g_{SiSi}(r)$ remains very small and close to unity, indicating that Si atoms are randomly dispersed in the Al host liquid. Table II in Ref. [45] gathers the first peak position value of all the partials. It is worth mentioning first that addition of a small amount of Mg and Si in pure Al leaves the first nearest distance unchanged with $r_{AlAl} = 2.7$ Å, close to pure liquid Al [33,60,61]. It also shows that r_{AlMg} is intermediate between r_{AlAl} and r_{MgMg}. The height of the first peak of $g_{AlMg}(r)$ is also intermediate. The same holds for r_{AlSi}, but in that case, the first peak of $g_{AlSi}(r)$ is higher than $g_{AlAl}(r)$ and $g_{SiSi}(r)$, showing a slightly higher affinity between Al and Si.

In order to investigate a potential ternary effect, AIMD simulations were performed for two binary alloys, namely $Al_{90}Mg_{10}$ and $Al_{90}Si_{10}$ in the same range of temperatures. The results for the partial pair-correlation functions are shown in Figs. S7 and S8, and the corresponding bond lengths are included in Table II in Ref. [45]. The same trends on the partials are seen, and only little change can be observed with respect to the ternary alloy. Nevertheless, addition of Si in Al-Mg binary alloys leads to the occurrence of a significant Mg-Si bonding in the ternary alloy as can be seen in Fig. 3(e). A similarity can be observed between the calculated Mg-Mg or Mg-Si distances and those reported for the Mg_2Si crystal structure, whose first neighbor distances are indicated by the vertical dashed lines in Figs. 3(d)–3(f). The bond-angle distribution in Fig. S9 of Ref. [45] also suggests short-range ordering compatible with precursors of this phase.

The resulting partial and total coordination numbers and their temperature evolution are represented in Fig. 4 for $Al_{80}Mg_{10}Si_{10}$. Only a modest increase of the total coordination numbers around Al, Mg, and Si is observed with decreasing temperature between $T = 1000$ and $T = 600$ K.
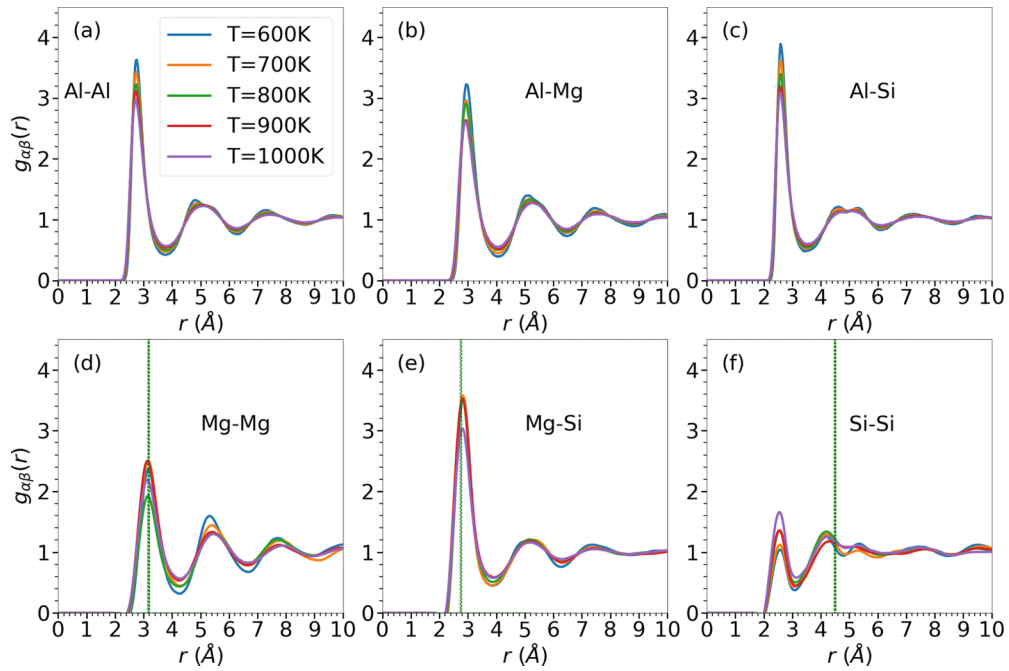
FIG. 3. Partial pair-correlation functions of $Al_{80}Mg_{10}Si_{10}$ liquid alloy for all studied temperatures by AIMD simulations. The green dashed vertical line indicates the first atomic distances of pairs in the Mg_2Si cubic crystal (The Materials Project [48]: reference mp-1367).

This mirrors the weak evolution of the first peak of the partial pair-correlation function. Structural changes are better revealed from the splitting of the partial-pair correlation function at the level of the second peak. This corresponds typically to a change of the orientational ordering as will be seen in the common-neighbor analysis below. The total coordination number of Al is: $N_c^{Al} = 12.4 \pm 0.2$, which is an intermediate value between $N_c^{Mg} = 15.0 \pm 0.2$ and $N_c^{Si} = 10 \pm 0.2$. Similar values for the total coordination numbers were found for the two binary liquid alloys (see Fig. S10 in Ref. [45]). For all liquid alloys (binary and ternary), the total coordination numbers show the following trend: $N_c^{Si} < N_c^{Al} < N_c^{Mg}$. Moreover, addition of 10% Mg and/or 10% Si leads to a significant

FIG. 4. Total and partial coordination numbers as function of temperature in the ternary $Al_{80}Mg_{10}Si_{10}$ liquid alloy. Uncertainties in the values are of the order of 0.2.

increase of coordination number around Al with respect to pure Al, whose values of N_c are between 11.6 and 11.8 in the present range of temperatures [33,61]. This feature implies (i) an increase of the compacity $\eta_{Al} = \pi \rho r_{max,AlAl}^3 / 6$, where $r_{max,AlAl}$ the position of the first peak and ρ is the atomic density as shown in Table II of Ref. [45], since the coordination sphere remains the same as mentioned above, and (ii) the possible appearance of a specific chemical short-range order. The following inequality, $N_c^{Si} < N_c^{Al} < N_c^{Mg}$, could indicate that, in general, the local structure around each species is different, characteristic of a structural heterogeneity. It is worth noting that Mg-Mg and Mg-Si partial coordination numbers are larger than 1, and for Al-Si it is equal to 1, whereas Si-Si coordination is almost negligible. This confirms that, in contrast with Si-Si bonding, Mg-Mg pairing is favored in both $Al_{90}Mg_{10}$ and $Al_{80}Mg_{10}Si_{10}$, and that Si atoms exhibit preferential coordination with Mg, as expected by the analysis of the corresponding partial pair-correlation function. This is characteristic of the appearance of a CSRO, the latter being revealed by means of the Warren-Cowley [62] order parameter, $\alpha_i = 1 - N_c^{i-Al}/x_{Al}(N_c^{i-i} + N_c^{i-Al})$, giving $\alpha_{Si} = -0.06$ in $Al_{90}Si_{10}$ and $\alpha_{Mg} = 0.04$ in $Al_{90}Mg_{10}$.

The SRO is further investigated by means of CNA [52] around each species for the binary and ternary liquid alloys. In Table I, results are gathered for two temperatures showing the most important bonded pairs determined from IS configurations. Five-fold symmetry is represented by the 555 pairs as well as the 554 ones, which are a distorted version of 555 [52]. A high degree of FFS characterizes the SRO of all alloys in the liquid at $T = 1000$ K, and becomes even more pronounced in the undercooled state at $T = 600$ K.

As a general observation, for all systems, the FFS around Mg is higher than around Al, while for Si it is lower. For Mg, the presence of 666 pairs could indicate the presence
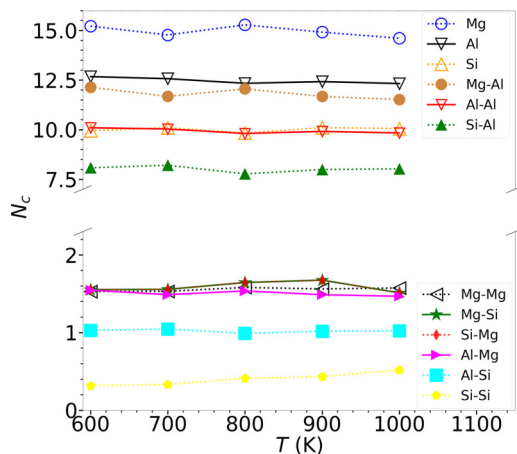
TABLE I. Common Neighbor Analysis for five Al-based liquid alloys calculated at $T = 1000$ and 600 K. Results for pure liquid Al, reported in Ref. [33], are also shown for comparison. The typical error bar for the calculated pair abundances are of the order of 0.01.

CNA (%)		$Al_{90}Mg_{10}$		$Al_{90}Si_{10}$		$Al_{80}Mg_{10}Si_{10}$			$Al_{70}Mg_{20}Si_{10}$			$Al_{70}Mg_{10}Si_{20}$		
$T = 1000$ K	Al [33]	Al	Mg	Al	Si	Al	Mg	Si	Al	Mg	Si	Al	Mg	Si
[5 5 5] + [5 4 4]	26.9	38.1	45.1	29.3	12.6	32.9	39.3	15.6	36.3	40.5	20.9	31.0	37.3	13.9
[6 6 6]	1.40	2.83	5.39	2.70	0.53	2.33	5.57	0.49	2.78	7.12	0.87	2.51	5.53	0.44
[4 4 4]	1.40	2.24	1.03	2.04	2.05	1.82	1.24	2.38	2.68	2.14	4.01	2.01	1.16	2.06
[4 3 3]	20.0	25.0	21.1	23.6	25.9	24.5	21.6	27.0	26.2	21.4	32.0	23.4	20.7	25.5
[4 2 2]	13.9	11.2	9.58	13.3	13.6	13.0	11.1	12.5	10.0	9.30	9.73	12.3	10.5	13.0
[4 2 1]	8.00	6.34	5.71	6.05	5.74	5.34	5.18	4.83	5.24	4.65	4.54	5.08	5.41	4.89
[3 2 2]	4.10	3.34	2.52	4.36	6.79	3.90	3.29	7.33	3.96	3.05	7.01	4.35	3.39	7.13
[3 1 1]	10.6	6.84	4.86	10.3	19.2	9.48	5.79	18.3	7.80	6.03	13.7	10.4	7.43	18.6
[3 0 0]	–	1.44	1.10	3.00	5.66	2.69	1.45	5.14	1.45	0.99	3.53	3.12	1.43	5.78
[2 0 0]	–	0.66	0.62	1.52	4.50	1.23	1.13	3.70	0.86	0.56	2.22	1.74	1.01	5.41
$T = 600$ K		Al	Mg	Al	Si	Al	Mg	Si	Al	Mg	Si	Al	Mg	Si
[5 5 5] + [5 4 4]	–	48.8	56.9	37.3	22.1	46.1	52.5	24.2	49.5	51.3	32.2	39.2	44.4	23.0
[6 6 6]	–	3.23	9.79	2.39	0.82	3.67	8.85	0.65	4.72	10.0	1.21	4.14	8.35	0.76
[4 4 4]	–	1.85	1.84	1.70	0.32	2.14	1.71	2.85	3.54	2.62	5.96	2.65	1.78	3.63
[4 3 3]	–	21.8	16.3	22.8	23.0	22.4	16.2	31.4	22.1	18.1	32.8	23.4	18.5	31.2
[4 2 2]	–	9.74	6.33	13.0	13.6	9.96	7.94	12.7	7.97	6.51	8.46	10.5	9.59	11.4
[4 2 1]	–	5.96	3.49	7.07	6.38	4.56	3.89	5.00	4.15	3.00	4.20	4.95	4.25	5.10
[3 2 2]	–	2.14	1.02	3.04	6.53	2.39	1.44	4.85	2.13	1.86	4.46	3.30	1.96	6.12
[3 1 1]	–	4.06	1.41	7.24	16.6	4.90	3.15	12.2	2.95	2.16	7.56	6.21	4.18	12.2
[3 0 0]	–	0.78	0.56	1.54	3.49	1.21	0.58	2.97	0.49	0.43	1.06	1.50	0.79	3.13
[2 0 0]	–	0.22	0.25	0.85	4.29	0.42	0.25	1.63	0.28	0.24	1.02	0.53	0.54	1.49

of bcc ordering when associated to 444 pairs. However, the proportion of 444 is too small, suggesting therefore Frank-Kasper polyhedra, mainly Z14 and Z15, to be more likely and consistent with a coordination number close to 15. For Si, the presence of 421 and 422 pairs is an indication of a significant cubic symmetry. The respective specific SRO around Mg and Si is reinforced in the undercooled regime. The 433 pairs can be associated either to very distorted 555 pairs or to distorted cubic symmetry. It generally decreases with decreasing temperature, indicating that the liquid becomes more structured. For both temperatures, the addition of Mg or Si atoms leads to a global increase of the FFS in each alloys by up to 10%, and sometimes even more around Al atoms with respect to pure liquid Al [33]. The increase of FFS around Al in alloys is consistent with a higher compacity, as mentioned above [15]. Table I also reports the presence of a small amount of 300 and 200 pairs in ternary alloys, also found in the Mg_2Si phase (see Table S3 in Ref. [45]) and consistently with the typical distances found in the partial-pair correlation functions and bond-angle distributions. Regarding the solubility phase diagram, Mg_2Si compound is in equilibrium with Al, and there is a quasi-binary line Al-Mg_2Si at the Mg:Si ratio of 1.73. The two binary invariant eutectic reactions occur for 12.5 wt% Si (liquid $\longrightarrow$ Al + Si) at 850 K, and for 34.5 wt% Mg (liquid $\longrightarrow$ Al + Al_8Mg_5) at 723 K. The ternary invariant reactions are liquid $\longrightarrow$ Al + Mg_2Si + Si at 828 K at nearly 5 wt% Mg and 13 wt% Si on one end, and liquid $\longrightarrow$ Al + Mg_2Si + Al_8Mg_5 at 722 K with 32.2 wt% Mg and 0.37 wt% Si on the other end. Note that the $Al_{10}Mg_{10}Si$ alloy lies beyond the solubility limit, meaning that the primary phase during solidification would be the Mg_2Si intermetallic

compound [63]. Nevertheless, it is difficult at this stage to claim the presence of precursors of the Mg_2Si phase that might form during slow solidification [64], given the small amount of these pairs present within the short time span of the simulations. This would require to perform large-scale MD simulations of the homogeneous nucleation process with a retrained ML potential [38], which is beyond the scope of the present paper.

Interestingly, addition of Mg in pure Al to form $Al_{90}Mg_{10}$ or Si to form $Al_{90}Si_{10}$ leads respectively to a global increase or decrease of ISRO. Then, adding Si in $Al_{90}Mg_{10}$ or adding Mg in $Al_{90}Si_{10}$ to form the ternary $Al_{80}Mg_{10}Si_{10}$ alloy follows the same trend, namely decreasing or increasing the FFS of the initial corresponding binary alloy. Finally, in the ternary alloys, the same rule holds again, as the FFS is favored globally and around Al when the Mg content is increased at constant Si composition and disfavored when Si content is increased at constant Mg composition. Therefore, modifying the respective compositions of Mg and Si affects the local order in Al-Mg-Si alloy. More particularly, adapting ISRO might impact diffusion [21], thereby contributing to control solidification morphology.

B. Structure-diffusion relationship

In order to determine self-diffusion coefficients for all the studied alloys, the mean-square-displacement $R_i^2(t)$ [Eq. (4)] is calculated for each species i on the production stage of the simulations after an equilibration of 30 ps. As can be easily seen on the log-log plot of the $R_i^2(t)$ curves in Figs. S24–S28 in Ref. [45], this physical quantity is divided into two main
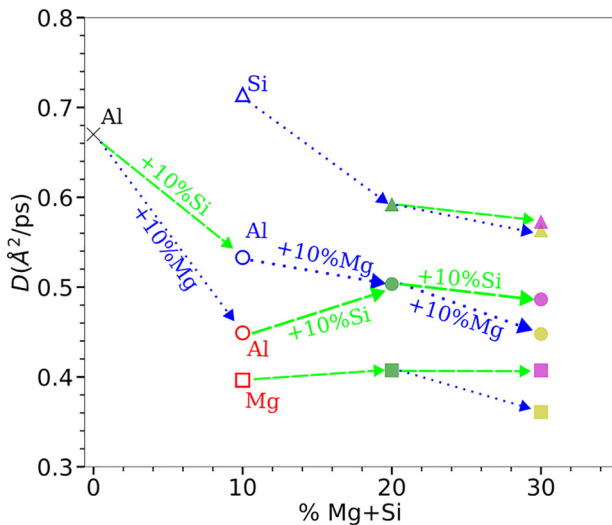
FIG. 5. Diffusion coefficients for all the liquid alloys as function of composition at $T = 1000$ K. The open symbols represent the binary liquid alloys (red: $Al_{90}Mg_{10}$; blue: $Al_{90}Si_{10}$) and the closed symbols represent ternary liquid alloys (green: $Al_{80}Mg_{10}Si_{10}$; dark yellow: $Al_{70}Mg_{20}Si_{10}$; magenta: $Al_{70}Mg_{10}Si_{20}$). Similar tendencies of diffusion coefficients have been found for other undercooling temperatures (see Figs. S29 and S30 in Ref. [45]). The cross represent the value for pure liquid Al from [33,37]. The global diffusion coefficient is 0.50 $Å^2$/ps for $Al_{80}Mg_{10}Si_{10}$, 0.45 $Å^2$/ps for $Al_{70}Mg_{20}Si_{10}$, and 0.49 $Å^2$/ps for $Al_{70}Mg_{10}Si_{20}$.

parts, starting at small times by the ballistic motions and followed by a linear diffusive regime roughly after $t = 20$ ps for all alloys. In time spans between the two regimes, a slowing down of the MSD can be seen, corresponding to the cage effects, which reinforces with decreasing temperature. The self diffusion coefficient is obtained by a linear regression of $R_i^2(t)$ in the long-time diffusive part and by using Eq. (5).

Results of diffusion coefficients are drawn as a function of composition at $T = 1000$ K (see Fig. 5). Starting from pure liquid Al, which was studied in a previous contribution [33], binary liquid alloys are obtained by adding Mg or Si respectively for $Al_{90}Mg_{10}$ and $Al_{90}Si_{10}$, leading to a downshift of diffusion coefficients of Al for both alloys. From the structural analysis in the preceding section, the enhancement of the compacity around Al atoms together with the more pronounced ISRO might be at the origin of this slowing down for the two binary alloys. Nevertheless, Fig. 5 clearly shows that adding Mg or Si in liquid Al does not yield to the same consequences. ISRO is more pronounced in $Al_{90}Mg_{10}$ than in $Al_{90}Si_{10}$ leading to lower diffusion of Al atoms. Moreover, in $Al_{90}Mg_{10}$ the higher icosahedral ordering around Mg atoms leads to an even lower value of D_{Mg}. For $Al_{90}Si_{10}$, the local ordering is rather cubic and less compact around Si giving rise to higher Si diffusion. It is worth mentioning that from AIMD simulation studies, Si is known as a fast diffuser [65], giving rise to a more important decoupling in the binary alloys. For both binaries, a decoupling of the self-diffusion coefficients is observed, which is more pronounced in $Al_{90}Si_{10}$, and might be a consequence of structural heterogeneities, as revealed by the CNA analysis. Such a decoupling also reveals dynamic heterogeneities as will be seen below.
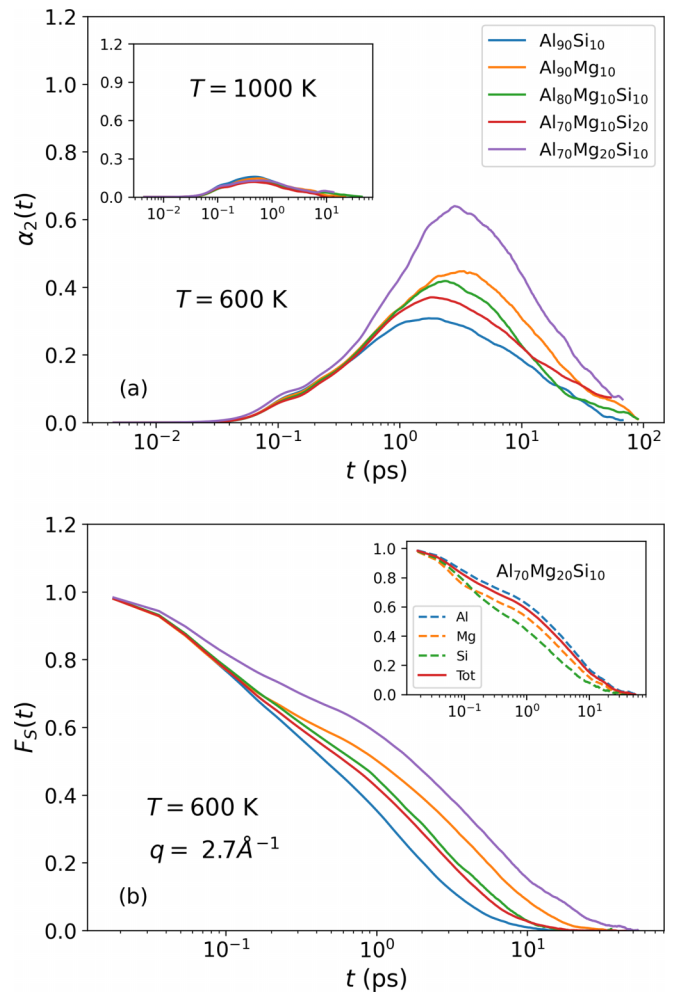

FIG. 6. Non-Gaussian parameter for all the liquid alloys at $T = 600$ K (a). The Inset corresponds to the same curves determined at $T = 1000$ K. Self-intermediate scattering function for all the liquid alloys at $T = 600$ K (b). A wave number $q = 2.7$Å corresponding roughly to the position of the first peak of the structure factor $S(q)$ is considered. The Inset corresponds to $F_S(\mathbf{q}, t)$ for $Al_{70}Mg_{20}Si_{10}$ along with the contributions of each species.

The $Al_{80}Mg_{10}Si_{10}$ ternary alloy can be formed, as mentioned above, either by adding Si in $Al_{90}Mg_{10}$ or adding Mg in $Al_{90}Si_{10}$, in substitution of Al atoms. Figure 5 shows that both paths are consistent with the mechanism unveiled above in which the increase of Mg content promotes ISRO and slows down the diffusion of each species, while the increase of Si composition induces cubic local ordering around Si and disfavors ISRO with the consequence of enhancing the diffusion of the species. This is all the more true for $Al_{70}Mg_{20}Si_{10}$ and $Al_{70}Mg_{10}Si_{20}$ obtained from $Al_{80}Mg_{10}Si_{10}$, respectively by increasing the Mg content at constant Si composition and increasing Si content and maintaining the Mg composition.

The global diffusion is marginally impacted by the substitution of Al by Si and/or Mg atoms in the studied composition range, which is consistent with previous works [66], while the difference in self-diffusion of the individual species is significant. Such a difference reveals dynamic heterogeneities, which can be quantified using the non-Gaussian parameter, $\alpha_2(t)$. The curves of $\alpha_2(t)$ of all the alloys are drawn

in Fig. 6(a) for the undercooled states at $T = 600$ K. They all display a significant positive amplitude, and thus reveal dynamic heterogeneities, as compared to those in the Inset determined at $T = 1000$ K, where only a small positive amplitude is seen, and mainly due to the cage effect that vanishes rapidly above 1 ps. The DHs then appear as a combined effect of the introduction of both Si and Mg elements. However, increasing the Mg content to 10% and 20% contribute the most to the DHs, with respect to $\alpha_2(t)$ for $Al_{90}Si_{10}$ displaying the smallest amplitude.

The corresponding self-intermediate scattering functions of all alloys are shown in Fig. 6(b), which give additional information on the structural relaxation process. At short times, typically below 0.1 ps, SISF shows a Gaussian-like behavior mirroring the ballistic regime seen in the corresponding MSD. In the undercooled region at $T = 600$ K, SISF reveals two relaxation mechanisms. The short-time one, usually referred to as the so-called β-relaxation and characterized by a shoulder, corresponds to the cage effect in the MSD. The final exponential decay to zero from this shoulder corresponds to a slower relaxation process referred as the so-called α relaxation. It should be noted that above the liquidus at $T = 1000$ K β-relaxation is absent, which can be seen in Fig. S31 Ref. [45], as only this exponential decay exists, being an indication of a homogeneous diffusion regime. It appears clearly in the undercooled states that additions of Mg leads to a increase of the structural relaxation time (α relaxation), whose values are given in Ref. [45]. It also gives rise to a more pronounced shoulder corresponding to an increase of the β-relaxation. The Inset of Fig. 6(b) illustrates the contribution of the individual species to the relaxation processes in the typical case of $Al_{70}Mg_{20}Si_{10}$, and shows that Mg and Al are at the origin of the β-relaxation, not seen for Si that relaxes much faster. This confirm the major role of Mg in the existence of dynamic heterogeneities in the ternary alloys studied here.

IV. CONCLUSION

In conclusion, AIMD simulations were conducted in the liquid and undercooled states for Al-rich Al-Mg-Si ternary system, prototypical of 6xxx alloys, together with their binary counterparts, namely Al-Mg and Al-Si, with the goal of understanding the relationship between structure and diffusion. Our results show that the presence of Mg and/or Si leads to a local structure around Al significantly more compact in the alloys than in pure Al, which has the consequence of a global lowering of the diffusion. Moreover, an opposite influence of Mg or Si addition in the alloys on the liquid structure and dynamics was found. Whereas the presence of Mg in the alloys promotes ISRO, Si atoms show a tendency to disfavor ISRO and to form a cubic local ordering. These effects are shown to impact the diffusion of all species depending on the respective Mg and Si contents, and suggest the mechanism by which an increase of Mg content generally slows down the diffusion of each species, while the increase of Si composition enhances their diffusion. This demonstrates that chemical short-range order (CSRO) between Mg and Si is able to neutralize the ISRO-killing effect of Si atoms without annihilating the ISRO-promoting effect of Mg atoms. The evidence of such an interplay between topological and chemical short range orders provides significant insight into alloy designing principles, as far as solidification morphology selection is concerned. It may constitute the basis of any future investigation of the effect of other additional elements to the structural and dynamic properties of this system, with the possibility to fine tune the compositions to control diffusion mechanisms and thus the solidification process.

ACKNOWLEDGMENTS

[1] R. Holmestad, R. Bjørge, F. J. H. Ehlers, M. Torsæter, C. D. Marioara, and S. J. Andersen, J. Phys.: Conf. Ser. **371**, 012082 (2012).

[2] H. W. Zandbergen, S. J. Andersen, and J. Jansen, Science **277**, 1221 (1997).

[3] C. Ravi and C. Wolverton, Acta Mater. **52**, 4213 (2004).

[4] A. G. Frøseth, R. Høier, P. M. Derlet, S. J. Andersen, and C. D. Marioara, Phys. Rev. B **67**, 224106 (2003).

[5] P. Jarry and M. Rappaz, C. R. Phys. **19**, 672 (2018).

[6] T. P. D. Lassance and F. Scheyvaerts, Eng. Fract. Mech. **73**, 1009 (2006).

[7] M. Mageto, *Al-Mg-Si Alloys: Micostructure, Hardness and Tensile Properties* (LAP LAMBERT Academic Publishing, 2010).

[8] J. A. Dantzig and M. Rappaz, *Solidification* (EPFL Press English Imprint, 2016).

[9] T. Iida and R. Guthrie, *The Physical Properties of Liquid Metals* (Oxford Science Publications, Clarendon Press, 1988).

[10] W. Sutherland, London, Edinburgh, Dublin Philos. Mag. J. Sci. **9**, 781 (1905).

[11] A. Einstein, Ann. Phys. (Berlin) **322**, 549 (1905).

[12] N. Jakse and A. Pasturel, Phys. Rev. B **94**, 224201 (2016).

[13] A. Pasturel and N. Jakse, Appl. Phys. Lett. **109**, 041904 (2016).

[14] D. Turnbull, J. Chem. Phys. **20**, 411 (1952).

[15] F. C. Frank, Proc. R. Soc. London A **215**, 43 (1952).

[16] P. Ronceray and P. Harrowell, Europhys. Lett. **96**, 36005 (2011).

[17] N. Jakse and A. Pasturel, Phys. Rev. Lett. **91**, 195501 (2003).

[18] S. Becker, E. Devijver, R. Molinier, and N. Jakse, Phys. Rev. B **102**, 104205 (2020).

[19] U. R. Pedersen, I. Douglass, and P. Harrowell, J. Chem. Phys. **154**, 054503 (2021).

[20] N. Jakse and A. Pasturel, Phys. Rev. B **78**, 214204 (2008).

[21] A. Pasturel and N. Jakse, npj Comput. Mater. **3**, 33 (2017).

[22] C. Tang and P. Harrowell, J. Chem. Phys. **148**, 044509 (2018).

[23] A. Pasturel and N. Jakse, Appl. Phys. Lett. **110**, 121902 (2017).

[24] N. Jakse and A. Pasturel, J. Chem. Phys. **143**, 084504 (2015).

[25] G. Kurtuldu, P. Jarry, and M. Rappaz, Acta Mater. **61**, 7098 (2013).

[26] G. Kurtuldu, Ph.D. thesis, Lausanne, EPFL (2014).

[27] G. Kurtuldu, P. Jessner, and M. Rappaz, J. Alloys Compd. **621**, 283 (2015).

[28] M. Rappaz, P. Jarry, G. Kurtuldu, and J. Zollinger, Metall. Mater. Trans. A **51**, 2651 (2020).

[29] N. Jakse and A. Pasturel, J. Chem. Phys. **141**, 234504 (2014).

[30] N. Jakse and A. Pasturel, AIP Adv. **7**, 105212 (2017).

[31] M. Bouhadja and N. Jakse, J. Phys.: Condens. Matter **32**, 104002 (2020).

[32] A. Pasturel, E. S. Tasci, M. H. F. Sluiter, and N. Jakse, Phys. Rev. B **81**, 140202(R) (2010).

[33] N. Jakse and A. Pasturel, Sci. Rep. **3**, 3135 (2013).

[34] J. Hafner, J. Comput. Chem. **29**, 2044 (2008).

[35] J. Behler, Chem. Rev. **121**, 10037 (2021).

[36] J. S. Smith, B. Nebgen, N. Mathew, J. Chen, N. Lubbers, L. Burakovsky, S. Tretiak, H. A. Nam, T. Germann, S. Fensin *et al.*, Nat. Commun. **12**, 1257 (2021).

[37] N. Jakse, J. Sandberg, L. F. Granz, A. Saliou, P. Jarry, E. Devijver, T. Voigtmann, J. Horbach, and A. Meyer, J. Phys.: Condens. Matter **35**, 035402 (2023).

[38] A. C. P. Jain, D. Marchand, A. Glensk, M. Ceriotti, and W. A. Curtin, Phys. Rev. Mater. **5**, 053805 (2021).

[39] G. Kresse and J. Hafner, Phys. Rev. B **47**, 558 (1993).

[40] G. Kresse and D. Joubert, Phys. Rev. B **59**, 1758 (1999).

[41] D. M. Ceperley and B. J. Alder, Phys. Rev. Lett. **45**, 566 (1980).

[42] T. Bryk, T. Demchuk, N. Jakse, and J.-F. Wax, Front. Phys. **6**, 6 (2018).

[43] F. Demmel, L. Hennet, and N. Jakse, Sci. Rep. **11**, 11815 (2021).

[44] L. Verlet, Phys. Rev. **159**, 98 (1967).

[45] See Supplementaal Material at http://link.aps.org/supplemental/10.1103/PhysRevB.108.224202 for some technical details;

partial structural factors of $Al_{90}Mg_{10}$; comparison of structure-dynamics results obtained by AIMD and HDNNP; $g_{\alpha\beta}(r)$ of $Al_{90}Mg_{10}$ and $Al_{90}Si_{10}$; comparison of bond angle distributions in the liquid $Al_{80}Mg_{10}Si_{10}$ alloy and in the Mg_2Si solid crystal; N_c for the two binary liquid alloys; atomic distances and the corresponding Al compacity; CNA results obtained for different crystal phases and for all liquid alloys; total and partial relaxation times and self-intermediate scattering functions; $R^2(t)$ for all liquid alloys; temperature and composition dependence of D. It also contains Refs. [33,37,43,46–48].

[46] T. E. Faber and J. M. Ziman, Philos. Mag. **11**, 153 (1965).

[47] Y. Waseda, M. Ohtani, and K. Suzuki, Z. Naturforsch. A **28**, 1002 (1973).

[48] https://materialsproject.org/materials/mp-1367?chemsys=Mg-Si.

[49] S. Nosé, J. Chem. Phys. **81**, 511 (1984).

[50] K. Binder and W. Kob, *Glassy Materials and Disordered Solids: An Introduction to Their Statistical Mechanics* (World scientific, Singapore, 2011).

[51] F. H. Stillinger and T. A. Weber, Phys. Rev. A **25**, 978 (1982).

[52] D. Faken and H. Jónsson, Comput. Mater. Sci. **2**, 279 (1994).

[53] A. Stukowski, Model. Simul. Mater. Sci. Eng. **18**, 015012 (2010).

[54] I.-C. Yeh and G. Hummer, J. Phys. Chem. B **108**, 15873 (2004).

[55] S. Mudry, A. Korolyshyn, and I. Shtablavyi, J. Phys.: Conf. Ser. **98**, 012016 (2008).

[56] J. Behler and M. Parrinello, Phys. Rev. Lett. **98**, 146401 (2007).

[57] A. Singraber, T. Morawietz, J. Behler, and C. Dellago, J. Chem. Theory Comput. **15**, 3075 (2019).

[58] T. Schenk, D. Holland-Moritz, V. Simonet, R. Bellissent, and D. M. Herlach, Phys. Rev. Lett. **89**, 075507 (2002).

[59] C. P. Royall and S. R. Williams, Phys. Rep. **560**, 1 (2015).

[60] N. A. Mauro, J. C. Bendert, A. J. Vogt, J. M. Gewin, and K. F. Kelton, J. Chem. Phys. **135**, 044502 (2011).

[61] M. M. G. Alemany, L. J. Gallego, and D. J. González, Phys. Rev. B **70**, 134206 (2004).

[62] J. M. Cowley, Phys. Rev. **77**, 669 (1950).

[63] L. F. Mondolfo, *Aluminum Alloys: Structure and Properties* (Butterworths, New Hampshire, 1976).

[64] Y. Liu, S. Kang, and H. Kim, Mater. Lett. **41**, 267 (1999).

[65] N. Jakse and A. Pasturel, Phys. Rev. B **79**, 144206 (2009).

[66] J. Qin, X. Li, J. Wang, and S. Pan, AIP Adv. **9**, 035328 (2019).